Deep and Low-Rank Quaternion Priors for Color Image Processing

Tingting Xu, Xiaoyu Kong, Qiangqiang Shen, Yongyong Chen, *Member, IEEE*, and Yicong Zhou, *Senior Member, IEEE*

***Abstract*— Due to the physical nature of color images, color image processing such as denoising and inpainting has shown extensive and versatile possibilities over grayscale image processing. The monochromatic and the concatenation model have been widely used to process color images by processing each color channel independently or concatenating three color channels as one unified one and then used existing grayscale image processing methods directly without specific operations. These above schemes, however, have some limitations: (1) they would destroy the inherent correlation among three color channels since they cannot represent color images holistically; (2) they usually focus on one specific handcrafted prior such as smoothness, low-rankness, or even deep prior and thus failing to fuse deep and handcrafted priors of color images flexibly. To conquer these limitations, we propose one unified model to integrate deep prior and low-rank quaternion prior (DLRQP) for color image processing under the plug-and-play (PnP) framework. Specifically, the quaternion representation with low-rank constraint is introduced to denote the color image in a holistic way and one advanced denoiser is adopted to explore the deep prior in an iterative process. To tightly approximate the quaternion rank, one nonconvex penalty function is further utilized. We derive an alternate iterative approach to tackle the proposed model. We empirically demonstrate that our model can achieve superior performance over existing methods on both color image denoising and inpainting tasks.**

***Index Terms*— Low-rank quaternion representation, deep prior, plug-and-play, color image denoising, color image inpainting.**

Manuscript received 4 October 2022; revised 9 December 2022; accepted 25 December 2022. Date of publication 2 January 2023; date of current version 3 July 2023. This work was supported in part by the National Natural Science Foundation of China under Grant 62106063, in part by the Guangdong Natural Science Foundation under Grant 2022A1515010819, in part by the Shenzhen College Stability Support Plan under Grant GXWD20201230155427003-20200824113231001, and in part by the Guangdong Provincial Key Laboratory of Novel Security Intelligence Technologies under Grant 2022B1212010005. This article was recommended by Associate Editor B. Wen. *(Corresponding author: Yongyong Chen.)*

Tingting Xu and Xiaoyu Kong are with the School of Computer Science and Technology, Harbin Institute of Technology (Shenzhen), Shenzhen 518055, China.

Qiangqiang Shen is with the School of Electronics and Information Engineering, Harbin Institute of Technology (Shenzhen), Shenzhen 518055, China.

Yongyong Chen is with the School of Computer Science and Technology, Harbin Institute of Technology (Shenzhen), Shenzhen 518055, China, and also with the Guangdong Provincial Key Laboratory of Novel Security Intelligence Technologies, Shenzhen 518055, China (e-mail: YongyongChen.cn@gmail.com).

Yicong Zhou is with the Department of Computer and Information Science, University of Macau, Macau, China.

Color versions of one or more figures in this article are available at https://doi.org/10.1109/TCSVT.2022.3233589.

Digital Object Identifier 10.1109/TCSVT.2022.3233589

I. Introduction

CAPTURING three color channels and enriching faithful representation of real scenes, color image processing has been widely applied in varied fields, such as color face recognition [1], color image encryption [2], color image denoising [3], [4], color image inpainting [5], [6], [7]. During the acquisition of color images, the image may contain mixed noise or miss some pixels due to the acquisition equipment or various other factors inevitably. In this paper, we mainly focus on two low-level color image processing tasks: color image denoising and color image inpainting, *i.e.*, recovering the latent color image from its noisy observation or incomplete one.

In previous studies, low-rank matrix approximation (LRMA) has been applied in numerous image processing applications [8], [9], [10], [11], [12], [13]. Its general process is to transform the image pixels of one spatial dimension in images as one column vector of the matrix and then utilize the low-rank attribute by an optimization algorithm to restore a clean image. Zhang et al. [10] proposed a modified Schatten-p norm minimization for accelerated matrix completion problem. Using non-local self-similarity, the low-rank matrix-based image restoration framework [12] was proposed. The multi-matrices low-rank decomposition model was developed for challenging image recovery problem [13]. Based on nonconvex nonsmooth rank (NNR), the work in [14] introduced a novel weighted NNR relaxation. In addition, Wang et al. [15] proposed the group sparse representation based on nonconvex weighted ℓ_p minimization. LRMA generally works well in some grayscale image-based applications [16], while the results based on LRMA methods may plummet when dealing with color images. The reason is that these LRMA methods tackle each color channel separately or concatenate three color channels and would destroy the strong correlation among three color channels [5]. In Fig. 1(a), we show how LRMA splits the three channels of a color image.

As an extension of two-dimensional matrix, tensor structure has gained keen attention in color images and higher-order data applications due to its capacity to preserve information in three dimensions simultaneously [17], [18], [19], [20]. For color images, the pixel values of three RGB color channels can be represented as three frontal slices of a tensor, as shown in Fig. 1(b). That is, one color image would be expressed as a three-order tensor. Most low-rank tensor

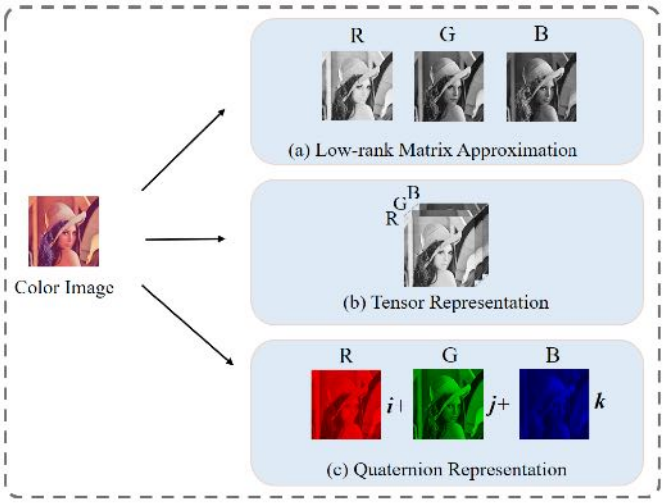

Fig. 1. The comparison among low-rank matrix approximation, quaternion representation and tensor representation.

approximation (LRTA)-based means can be summarized into two groups: 1) tensor decomposition-based methods; 2) tensor rank minimization-based methods. In the first one, a higher-order tensor can be decomposed into the product of two or more smaller ones, reducing the computational cost in this way [17], [21], [22]. The classic examples are the CANDECOMP/PARAFAC (CP) decomposition based methods [23] and the Tucker decomposition based methods [24]. Recently, Zhao et al. proposed to use tensor train decomposition [25] and denoisers to achieve tensor completion [26]. The second way is generally implemented by the regularization term of the tensor rank approximation, such as the tensor nuclear norm (TNN) [18], [20]. This is because minimizing the tensor rank is an NP-hard problem, and the TNN can be utilized as a compact convex substitution of the tensor rank. Tensor completion methods based on TNN [27], [28] have been extensively studied. Nevertheless, methods of the first type are inevitable to pre-define the tensor rank, but how to determine an accurate rank in practice is still a challenging problem [29]. Methods of the second category overcome the above method, yet with high computational bottleneck.

Another promising way to express color images is the recently popular quaternion representation [30], in which quaternion, as extension of imaginary number, includes one real component and three imaginary components. To seamlessly denote the color images, quaternion representation (QR) uses one pure quaternion number with three imaginary components to store three color channels [31]. In Fig. 1, we show the comparison among low-rank matrix approximation, tensor representation, and quaternion representation. Thus, the main advantage of QR is that the three color channels simultaneously are treated by QR representation, which can well keep the connection between image colors and achieve superior performance in color image processing applications [1], [30], [32], [33], [34], [35], [36], [37]. For example, Xu et al. proposed a novel approach based on quaternion-based dictionary learning model to restore color image [34]. Zou et al. used quaternion collaborative and sparse representation to preserve the color structures [1]. Besides, a new quaternion based sparse regression algorithm was put forward to enhance robustness for two-dimensional quaternion principle component analysis [35]. Compared to tensor representation-based methods, QR-based methods can not only fully utilize color information, but preserve the orthogonal character for the coefficients of three channels, which attains a structured representation [34]. Although current QR-based color image processing methods could represent color images well, they still incorporate some other prior knowledge. The studies in [5], [33], [38], and [39] extended the popular LRMA variants, such as matrix factorization, Geman function, weighted nuclear norm into quaternion representation. Huang et al. [40] proposed the quaternion extension of dictionary learning algorithm and total variation to recovery color image.

Owing to the powerful representation learning capability of deep learning, deep convolutional neural network (CNN)-based grayscale and color image methods have been developed and achieved promising performance [3], [37], [41], [42]. While much of the research into color image denoising and inpainting usually focuses on one specific handcrafted prior such as smoothness [43], low-rankness [32], sparsity [44] or even deep prior [41] but unfortunately fails to fuse deep and handcrafted priors of color images flexibly and simultaneously.

Thus, we consider the possibility to develop one unified method combining two popular color image priors. Meanwhile, the matrix representation for the color image destroys the inherent structural information. Compared to tensor representation, QR is considered to be integrated into this framework since QR preserves the orthogonal character for the coefficients of three channels, which attains a structured representation while preserving structural information. Therefore, we consider introducing quaternion representation to provide a novel way to model color images while using a unified framework of low-rank and deep priors. To achieve this goal, we intend to propose a novel low-rank quaternion representation method with a deep image prior (DLRQP) for color image denoising and inpainting, which integrates low-rank quaternion prior and deep prior into one unified framework. In DLRQP, the low-rank quaternion and deep priors are explored in a mutual promotion manner. Consequently, DLRQP inherits the good interpretability of low-rank prior, powerful structure retention of quaternion representation, and strong learning capability of deep prior. Specifically, DLRQP utilizes the flexible plug-and-play (PnP) framework to incorporate an advanced denoiser and low-rank quaternion representation in an iterative process. Besides, DLRQP also exploits a nonconvex function to obtain a better approximation of the quaternion rank. The contributions of this work mainly include as follows:

- We propose the synchronous integrated deep prior and low-rank quaternion prior method (DLRQP) for color image processing, which probes the global property and local characterization of color images deeply and simultaneously.
- Different from existing QR-based methods that only focus on low-rank property or utilize deep conventional prior, DLRQP integrates a deep learning-based denoiser

and low-rank quaternion representation under the PnP framework. A flexible and efficient solver based on the alternating direction method of multipliers (ADMM) is also developed.
- Concretely speaking, we further extend DLRQP to deal with color image denoising and inpainting tasks. Experiments on color images are carried out and the results clearly confirm that the proposed DLRQP is superior to several competing methods on these two tasks.

The rest parts of this paper are organized as follows. We review several notations and preliminary knowledge in Section II. Section III provides the proposed DLRQP model, extends DLRQP for color image denoising and color image inpating and devises the ADMM-based algorithms. Section IV conducts experiments to verify the effectiveness of the proposed DLRQP method on color image denoising and inpainting tasks. Finally, this article is concluded in Section V.

II. Notations and Preliminaries

In this section, we briefly give several notations and preliminary knowledge about quaternion algebra and plug-and-play framework used in our paper.

A. Notations and Quaternion Algebra

We summarize several necessary notations and real number algebra in Table I. Quaternion space $\mathbb{H}$, an extension of real and complex spaces, is a mathematical concept invented by Hamilton in 1843 [45]. Given a quaternion number $\dot{a}$, we can express it in the form of one real part and three imaginary parts, *i.e.*,

$$\dot{a} = a_0 + a_1\mathbf{i} + a_2\mathbf{j} + a_3\mathbf{k}, \tag{1}$$

where $a_i \in \mathbb{R}$ ($i = 0, 1, 2, 3$) are real numbers and $\mathbf{i}$, $\mathbf{j}$, $\mathbf{k}$ denotes three imaginary units. In particular, if a_0 is equal to zero, $\dot{a}$ is called a pure quaternion. Similar to complex numbers, quaternion addition or subtraction simply add or subtract components, *i.e.*,

$$\dot{a} \pm \dot{b} = (a_0 \pm b_0) + (a_1 \pm b_1)\,\mathbf{i} + (a_2 \pm b_2)\,\mathbf{j} + (a_3 \pm b_3)\,\mathbf{k}. \tag{2}$$

It should be noted that in general, the product of quaternions does not satisfy the commutative law, *i.e.*, $\dot{a}\dot{b} \neq \dot{b}\dot{a}$.

Given a quaternion $\dot{a} = a_0 + a_1\mathbf{i} + a_2\mathbf{j} + a_3\mathbf{k}$, its conjugate and modulus are expressed as $\dot{a}^* = a_0 - a_1\mathbf{i} - a_2\mathbf{j} - a_3\mathbf{k}$ and $|\dot{a}| = \sqrt{a_0^2+a_1^2+a_2^2+a_3^2}$. $\dot{a}^{-1}$ represents the inverse of $\dot{a}$, and $\dot{a}^{-1}\dot{a} = \dot{a}\dot{a}^{-1} = 1$.

Analogously, given a quaternion matrix $\dot{\mathbf{A}} = \mathbf{A}_0 + \mathbf{A}_1\mathbf{i} + \mathbf{A}_2\mathbf{j} + \mathbf{A}_3\mathbf{k}$, where $\mathbf{A}_i \in \mathbb{R}^{M\times N}$ ($i = 0, 1, 2, 3$), its conjugate, transpose and conjugate transpose are defined as $\dot{\mathbf{A}}^* = (\dot{a}^*_{i,j})$, $\dot{\mathbf{A}}^T = (\dot{a}_{j,i})$, $\dot{\mathbf{A}}^{\mathrm{H}} = (\dot{a}^*_{j,i})$, respectively, where $1 \le i \le M$, $1 \le j \le N$. The Frobenius norm of $\dot{\mathbf{A}}$ is denoted as $\|\dot{\mathbf{A}}\|_F = \sqrt{\sum_{i=1}^{M}\sum_{j=1}^{N}|\dot{a}_{i,j}|^2}$.

Quaternion matrices are widely employed to transform them from the quaternion domain into the complex adjoint form, *i.e.*, $\dot{\mathbf{A}} = \mathbf{A}_x + \mathbf{A}_y\mathbf{j}$ [46] where $\mathbf{A}_x$, $\mathbf{A}_y \in \mathbb{C}^{M\times N}$. We use P to denote the operation of converting the quaternion form into the complex form, then the complex representation form of $\dot{\mathbf{A}} \in \mathbb{R}^{M\times N}$ is expressed as

$$P_{\dot{\mathbf{A}}} = \begin{bmatrix} \mathbf{A}_x & \mathbf{A}_y \\ -\mathbf{A}_y^* & \mathbf{A}_x^* \end{bmatrix} \in \mathbb{C}^{2M\times 2N}. \tag{3}$$

For more details on quaternion algebra, one can refer to [46] and [47].

TABLE I
Basic Notations

Notations	Explanations
$\mathbb{R}$, $\mathbb{C}$, $\mathbb{H}$	Real space, complex space, quaternion space.
a, $\mathbf{a}$, $\mathbf{A}$, $\mathcal{A}$	Scalar, vector, matrix, tensor.
$\dot{a}$, $\dot{\mathbf{a}}$, $\dot{\mathbf{A}}$	Quaternion scalar, Quaternion vector, and Quaternion matrix.
$\mathbf{I_n} \in \mathbb{R}^{n\times n}$	Identity matrix.
$\mathcal{A}_{ijk}$	The (i,j,k)-th entry of $\mathcal{A}$.
$\mathcal{A}(:,:,k)$ or $\mathcal{A}^{(k)}$	The k-th frontal slice of $\mathcal{A}$.
$\mathrm{Tr}(\mathbf{A}) = \sum_{i=1}^{n} x_{ii}$	The trace of $\mathbf{A} \in \mathbb{R}^{n\times n}$.
$\langle \mathcal{A},\mathcal{B}\rangle = \sum_{ijk} x_{ijk}y_{ijk}$	The inner product of $\mathcal{A}$ and $\mathcal{B}$.
$\|\mathcal{A}\|_F^2 = \sum_{ijk} \mathcal{A}_{ijk}^2$	The Frobenius norm of $\mathcal{A}$.
$\|\mathcal{A}\|_1 = \sum_{ijk} \|\mathcal{A}_{ijk}\|$	The ℓ_1-norm of $\mathcal{A}$.

Following the quaternion singular value decomposition (QSVD) [46], the definitions of quaternion rank and quaternion nuclear norm can be given:

Definition 1 (Quaternion Rank): [5]: For a quaternion matrix $\dot{\mathbf{A}}\dot{\mathbf{A}} \in \mathbb{H}^{M\times N}$, the number n of nonzero singular values is represented as the rank, where $n < min\{M, N\}$.

Definition 2 (Quaternion Nuclear Norm (QNN)): [5]: QNN of a quaternion matrix $\dot{\mathbf{A}} \in \mathbb{H}^{M\times N}$, expressed as $\|\dot{\mathbf{A}}\|_{\mathrm{QNN}}$, is the sum of all nonzero singular values, *i.e.*, $\|\dot{\mathbf{A}}\|_{\mathrm{QNN}} = \sum_i \sigma_i(\dot{\mathbf{A}})$.

Similar to the nuclear norm in the real domain, the quaternion nuclear norm is also the convex substitution of the quaternion rank [5]. To tackle such convex optimization problem on quaternions, we introduce the following theorem:

Theorem 1 (Quaternion Singular Value Thresholding (QSVT)): [5]: Given an arbitrary quaternion matrix $\dot{\mathbf{A}} \in \mathbb{H}^{M\times N}$ and a positive real number λ, the QSVT method can be expressed as follows:

$$\hat{\dot{\mathbf{B}}} = \dot{\mathbf{U}} S_\lambda(\Sigma) \dot{\mathbf{V}}^H, \tag{4}$$

where $\dot{\mathbf{U}}, \Sigma, \dot{\mathbf{V}}$ are from the QSVD of the quaternion matrix $\dot{\mathbf{A}}$, and $S_\lambda(\Sigma) \in \mathbb{R}^{M\times N}$ is denoted as $S_\lambda(\Sigma) = diag(\max\{\sigma_i(\dot{\mathbf{A}}\dot{\mathbf{A}}) - \lambda, 0\})$.

B. Low-Rank Matrix Approximation

The main aim of the LRMA is to recover a high-quality image $\mathbf{X}$ from the noisy observation $\mathbf{A}$, and the optimization problem can be formulated as:

$$\min_{\mathbf{X}} \lambda * \mathbf{Rank}\,(\mathbf{X}) + \frac{1}{2}\|\mathbf{X} - \mathbf{A}\|_F^2, \tag{5}$$

where $\mathbf{Rank}(\cdot)$ is the rank function, and $\lambda > 0$ is a regularization parameter. The first term named regularization term is to impose the low-rank property of the image to

constrain the model. The second term, *i.e.*, data fidelity term constrains the discrepancy between X and A to be as small as possible.

Since the rank minimization problem in Eq. (5) is usually NP-hard, the nuclear norm was put forward to approximate the matrix rank, which proved that the nuclear norm is the tightest convex relaxation [48]. Various heuristic convex and nonconvex surrogates were proposed [11], [49], [50].

C. Plug-and-Play Framework

The PnP framework was first discovered in [51], which utilized advanced denoising algorithms as implicit priors plugged into the forward model, providing a flexible and efficient way to deal with various inverse problems. Under the ADMM framework, all variables could be decoupled into several subproblems. Therefore, the solution process of the ADMM framework has a modular structure, in which the subproblem utilized to deal with the prior regularization term can be written as:

$$x = \arg\min_{x} \Phi(x) + \frac{1}{2\sigma^2}\|x - y\|^2, \tag{6}$$

where $\Phi(x)$ represents the prior term; y can be regarded as a noisy image. Eq. (6) can be expressed as a denoising problem. Therefore, this denoising module can be replaced with the off-the-shelf denoising algorithm. The PnP framework has shown excellent reconstruction capability in numerous applications, including deblurring [52], restoration [53], [54], super-resolution [55] and demosaicing [56].

III. The Proposed Deep and Low-Rank Quaternion Priors (DLRQP) Model

We first propose the DLRQP model based on deep and nonconvex low-rank quaternion priors. Then, we extend the proposed model into two classic color image processing tasks, namely color image denoising and color image inpainting, and propose the ADMM-based algorithms.

A. The Proposed DLRQP Model

When handling color image processing tasks, previous LRMA method in Eq. (5) usually exploited either monochromatic model or the concatenation model. That is, the former model processes each color channel of color images independently while the second model concatenates three color channels as one unified one and finally they used existing grayscale image processing methods directly without specific operations. However, they would destroy the inherent correlation among three color channels since they cannot represent color images holistically. Although the improvement has been made by the recently proposed low-rank quaternion approximation [11] and CNN-based methods [41], these methods focus on one specific prior knowledge such as smoothness [43], low-rankness [32], or even deep prior [41], but unfortunately fail to fuse deep and handcrafted priors of color images flexibly.

Meanwhile, we consider utilizing the prior knowledge, which is obtained from deep learning-based ways and low-rank quaternion representation. Inspired by the huge success of Convolutional Neural Networks (CNNs) in image restoration, we consider incorporating the powerful strength of CNNs to capture details as a compensation for restoring underlying images. In this paper, we intend to integrate the strengths between low-rank priors based on quaternion representation and deep learning-based image priors. As a consequence, our DLRQP model can be expressed as follows:

$$\min_{\dot{\mathbf{X}}} \dot{\mathbf{A}}\lambda * \mathbf{Rank}\left(\dot{\mathbf{X}}\right) + \alpha\Phi(\mathcal{X}) + \frac{1}{2}\|\dot{\mathbf{X}} - \dot{\mathbf{A}}\|_F^2, \tag{7}$$

where $\alpha > 0$ is a regularization parameter, and $\mathcal{X} \in \mathbb{R}^{M\times N\times 3}$ represents the tensor form of the recovered color image. $\dot{\mathbf{X}} \in \mathbb{H}^{M\times N}$ and $\dot{\mathbf{A}} \in \mathbb{H}^{M\times N}$ represent the constructed quaternion matrix and the observed quaternion matrix, respectively. The tensor $\mathcal{X}$ and the quaternion matrix $\dot{\mathbf{X}}$ are different representations of the same color image. We can define an operator $\hbar : \mathbb{R}^{M\times N\times 3} \mapsto \mathbb{H}^{M\times N}$, which enables the conversion between tensor and quaternion, *i.e.*, $\dot{\mathbf{X}} = \hbar(\mathcal{X})$ and $\mathcal{X} = \hbar^{-1}(\dot{\mathbf{X}})$. $\hbar^{-1}$ is the inverse of $\hbar$. Specifically, this operator can be expressed as $\dot{\mathbf{X}} = \mathcal{X}(:,:,1)\mathbf{i} + \mathcal{X}(:,:,2)\mathbf{j} + \mathcal{X}(:,:,3)\mathbf{k}$. $\mathbf{Rank}(\cdot)$ denotes the quaternion rank function. $\Phi(\mathcal{X})$ denotes an implicit regularizer, and we can plug an advanced denoiser as deep image prior. Instead of using CNNs to build network structures and perform end-to-end training, a denoising CNN trained on a large number of natural images as the implicit prior is plugged in existing model directly. In summary, our model is more flexible and economical to deal with different application scenarios.

To tackle the NP-hard issue, we adopt the Laplace function as the nonconvex rank function to better approximate the quaternion rank and further formulate Eq. (7) as

$$\min_{\dot{\mathbf{X}}} \lambda * \|\dot{\mathbf{X}}\|_{\gamma,\mathrm{QNN}} + \alpha\Phi(\mathcal{X}) + \frac{1}{2}\|\dot{\mathbf{X}} - \dot{\mathbf{A}}\|_F^2, \tag{8}$$

where $\gamma > 0$ is a constant, which is the Laplace parameter. Specifically, the Laplace function in QNN can be expressed as follows:

$$\begin{aligned}\|\dot{\mathbf{X}}\|_{\gamma,\mathrm{QNN}} &= \sum_i \phi(\sigma_i(\dot{\mathbf{X}}), \gamma) \\ &= \sum_i \phi(1 - e^{-\sigma_i(\dot{\mathbf{X}})/\gamma}),\end{aligned} \tag{9}$$

where $\phi(x) = 1 - e^{x/\gamma}$ denotes the Laplace function, and $\sigma_i(\cdot)$ denotes the i-th singular value of the quaternion rank. Next, we discuss the concrete representation of the proposed DLRQP model in specific color image processing tasks.

B. DLRQP for Color Image Denoising

We first use the proposed DLRQP model to solve the color image denoising task, whose main aim is to estimate the original color image $\mathcal{X}$ by restraining the noise ϵ from the observed color image $\mathcal{A}$. The corresponding model is expressed as:

$$\mathcal{A} = \mathcal{X} + \epsilon. \tag{10}$$

In generally, ϵ is the additive white Gaussian noise, and its mean is zero and the variance is τ^2. Since this type

of inversion problem is ill-posed, some priors should be explored as regularization terms in the solution model to obtain satisfactory denoising performance. In this part, we propose a novel denoising model, which simultaneously considers local, nonlocal, and global prior information of color images.

In the proposed model, we employ nonlocal self-similarity (NSS) to characterize the nonlocal information of color images. NSS is widely utilized in image processing problems by clustering similar patches into a group [57], [58]. Zha et al. further proposed to combine NSS and group sparsity residual constraint to deal with various image processing tasks [59]. Xie et al. utilized pixel weighting strategy and NSS to explore the global and nonlocal information of the image [60]. In this subsection, we consider quaternion representation combined with NSS to construct nonlocal priors for images. Specifically, the original color image is divided into many small patches with size of $n_1 \times n_2 \times 3$. By using the operator $\hbar$, we represent each patch as a quaternion matrix and stretch it into a column vector, *i.e.*, $\dot{\mathbf{a}}_i \in \mathbb{H}^{n_1 n_2}$, and its similar patch group is constructed by searching for the m closest image patches within a given searching window. It is worth noting that the m similar patches contain $\dot{\mathbf{a}}_i$. A quaternion matrix, $\dot{\mathbf{A}}_i = [\dot{\mathbf{a}}_{1i}, \dot{\mathbf{a}}_{i2}, \cdots, \dot{\mathbf{a}}_{im}] \in \mathbb{H}^{n_1 n_2 \times m}$, is utilized to store these similar patches.

Global correlation is characterized by the low-rankness of similar patch groups. NSS follows the assumption that there exist many image patches similar to the exemplar patch in the natural image. Based on this, we also assume that the quaternion matrix $\dot{\mathbf{A}}_i$ we constructed as aforementioned is of low rank. Meanwhile, we utilize an implicit regularization term on the whole image to plug a denoising CNN to preserve local details. By formulating a novel color image denoising framework in the quaternion domain that can use these local, nonlocal, and global priors simultaneously, we give the following optimization

$$\min_{\dot{\mathbf{X}}} \|\dot{\mathbf{X}}\|_{\gamma,\mathrm{QNN}} + \alpha\Phi(\mathcal{X}) + \frac{1}{\tau^2}\|\dot{\mathbf{X}} - \dot{\mathbf{A}}\|_F^2, \tag{11}$$

where $\|\dot{\mathbf{X}} - \dot{\mathbf{A}}\|_F^2$ is the data fidelity term utilized to constrain the model to conform to the image degradation process in Eq. (10). Different from Eq. (7), here $\dot{\mathbf{X}} \in \mathbb{H}^{n_1 n_2 * m}$ represents a quaternion matrix composed of similar patches. In addition, the l_2-norm has a good performance in suppressing Gaussian noise. $\Phi(\mathcal{X})$ is an implicit regularization term, which is tackled by the denoising CNN under the PnP framework. Different from existing denoising methods, our proposed model is based on quaternion representation, which can better characterize the structural information of color images. Then we explore three different types of priors that simultaneously leverage the model so that they can benefit from each other. Moreover, we introduce the deep learning-based denoiser under the PnP framework, which has greater flexibility and generalization ability applied to different scenarios and applications than directly designing a network structure. The proposed DLRQP model in (11) imposes the low-rank constraint on the similar patch group $\dot{\mathbf{X}}$ to explore the NSS property while the deep prior is investigated on the whole image $\mathcal{X}$.

Then, we utilize ADMM and PnP framework to solve the problem (11). An auxiliary variable $\mathcal{Z} \in \mathbb{R}^{M\times N\times 3}$ is introduced, and the minimization problem (11) can be rewritten as

$$\begin{aligned} &\min_{\dot{\mathbf{X}},\mathcal{Z}} \quad \|\dot{\mathbf{X}}\|_{\gamma,\mathrm{QNN}} + \alpha\Phi(\mathcal{Z}) + \frac{1}{\tau^2}\|\dot{\mathbf{X}} - \dot{\mathbf{A}}\|_F^2, \\ &s.t. \quad \mathcal{Z} = \mathcal{X}. \end{aligned} \tag{12}$$

The relevant augmented Lagrangian function of Eq. (12) is expressed as

$$\begin{aligned} \mathcal{L}_\mu(\dot{\mathbf{X}}, \mathcal{Z}; \Lambda) = \|\dot{\mathbf{X}}\|_{\gamma,\mathrm{QNN}} + \alpha\Phi(\mathcal{Z}) + \frac{1}{\tau^2}\|\dot{\mathbf{X}} - \dot{\mathbf{A}}\|_F^2 \\ + \frac{\mu}{2}\|\mathcal{X} - \mathcal{Z} + \frac{\Lambda}{\mu}\|_F^2, \end{aligned} \tag{13}$$

where $\Lambda \in \mathbb{R}^{M\times N\times 3}$ and μ are the Lagrangian multiplier and the penalty parameter, respectively. Then, Eq. (13) can be tackled by updating all variables iteratively.

$\dot{\mathbf{X}}$ sub-problem: The $\dot{\mathbf{X}}$ at k-th iteration is updated by

$$\begin{aligned} \dot{\mathbf{X}}^{k+1} = \arg\min_{\dot{\mathbf{X}}} \|\dot{\mathbf{X}}\|_{\gamma,\mathrm{QNN}} + \frac{1}{\tau^2}\|\dot{\mathbf{X}} - \dot{\mathbf{A}}\|_F^2 \\ + \frac{\mu}{2}\|\mathcal{X} - \mathcal{Z}^k + \frac{\Lambda^k}{\mu^k}\|_F^2, \end{aligned} \tag{14}$$

where $\dot{\mathbf{X}} \in \mathbb{H}^{n_1 n_2 \times m}$ represents a quaternion matrix composed of nonlocal similar patches of the exemplar patch, and $\mathcal{X} \in \mathbb{R}^{M\times N\times 3}$ is the full-sized color image. For ease of calculation, when updating $\dot{\mathbf{X}}$, we also take the nonlocal similar pathes with the same position and number for $\mathcal{X}$, $\mathcal{Z}$, Λ, to construct a quaternion matrix, then Eq. (14) can be rewritten as

$$\begin{aligned} \dot{\mathbf{X}}^{k+1} &= \arg\min_{\dot{\mathbf{X}}} \|\dot{\mathbf{X}}\|_{\gamma,\mathrm{QNN}} + \frac{1}{\tau^2}\|\dot{\mathbf{X}} - \dot{\mathbf{A}}\|_F^2 \\ &\quad + \frac{\mu}{2}\|\dot{\mathbf{X}} - \dot{\mathbf{Z}}^k + \frac{\dot{\Lambda}^k}{\mu^k}\|_F^2 \\ &= \arg\min_{\dot{\mathbf{X}}} \|\dot{\mathbf{X}}\|_{\gamma,\mathrm{QNN}} \\ &\quad + \beta\|\dot{\mathbf{X}} - \frac{(\mu^k\dot{\mathbf{Z}}^k - \dot{\Lambda}^k)\tau^2 + 2\dot{\mathbf{A}}}{2 + \mu\tau^2}\|_F^2, \end{aligned} \tag{15}$$

where $\beta = \frac{2+\mu\tau^2}{2\tau^2}$. To tackle the issue, Chen et al. [5] introduced the difference of convex algorithm (DCA) for the following nonconvex optimization:

$$\min_{\dot{\mathbf{X}}} \lambda * \|\dot{\mathbf{X}}\|_{\gamma,\mathrm{QNN}} + \frac{1}{2}\|\dot{\mathbf{X}} - \dot{\mathbf{B}}\|_F^2. \tag{16}$$

Then, we introduce the following Theorem to give the solution to the above optimization.

Theorem 2: [5]: Given a quaternion matrix $\dot{\mathbf{B}} \in \mathbb{H}^{M\times N}$, its QSVD is defined as $\dot{\mathbf{B}} = \dot{\mathbf{U}}S\dot{\mathbf{V}}^H$ and $S = diag(\sigma_{\dot{\mathbf{B}}})$. The global optimal solution of Eq. (16) is $\hat{\dot{\mathbf{X}}} = \dot{\mathbf{U}}\hat{S}\dot{\mathbf{V}}^H$, where $\hat{S} = diag(\hat{\sigma})$. The $\hat{\sigma}$ can be acquired by

$$\hat{\sigma} = \arg\min_{\sigma\geq 0} \lambda * \phi(\sigma, \gamma) + \frac{1}{2}\|\sigma - \sigma_{\dot{\mathbf{B}}}\|_2^2. \tag{17}$$

Since $\phi(\cdot)$ is the nonconvex function, which is continuous, differentiable, monotonically nondecreasing on $[0, +\infty)$, and

concave with respect to σ, it is not easy to tackle the problem (17) directly. The DCA aims to iteratively optimize the difference of two convex functions by linearizing the concave term, which is transformed from the original non-convex function. Heuristically, we utilize the DCA to tackle Eq. (17) and in the $(k+1)$-th iteration we obtain the following formula:

$$\sigma^{k+1} = \arg\min_{\sigma \geq 0} \lambda * \nabla\phi(\sigma^k)^T\sigma + \frac{1}{2}\|\sigma - \sigma_{\dot{\mathbf{B}}}\|_2^2, \quad (18)$$

where $\nabla\phi(\sigma^k)^T$ denotes the gradient of $\phi(\cdot)$ at σ^k. We can get the following closed-form solution of Eq. (18)

$$\sigma^{k+1} = (\sigma_{\dot{\mathbf{A}}} - \lambda * \nabla\phi(\sigma^t))_+. \quad (19)$$

After repetitious iterations, DCA will eventually converge to $\hat{\sigma}$ which is the local optimal point, and then $\hat{\dot{\mathbf{X}}} = \dot{\mathbf{U}}diag(\hat{\sigma})\dot{\mathbf{V}}^H$. The entire procedure of handling the Eq. (16) is summarized in Algorithm 1.

Algorithm 1 Solving Problem (16) Using DCA

Input: The quaternion matrix $\dot{\mathbf{B}} \in \mathbb{H}^{M\times N}$, parameter $\lambda > 0$.
Initialization: $k = 0$, $\sigma = 0$.
1: **repeat**
2: Calculate the gradient of $\phi(\cdot)$;
3: Update σ^{k+1} via Eq. (19);
4: **until** converge
Output: The reconstructed tensor $\mathcal{X}$.

$\mathcal{Z}$ **sub-problem**: After Eq. (15) is updated, we get a clean pacth group $\dot{\mathbf{X}}$ and then convert $\dot{\mathbf{X}}$, $\dot{\mathbf{Z}}$, $\dot{\Lambda}$ into real number matrices, and concatenate all the patches to obtain $\mathcal{X}$, $\mathcal{Z}$, Λ with the same size of the original image, respectively. Fixing the rest variables, $\mathcal{Z}$ is updated by addressing the subproblem

$$\mathcal{Z}^{k+1} = \arg\min_{\mathcal{Z}} \alpha\Phi(\mathcal{Z}) + \frac{\mu}{2}\|\mathcal{Z} - \left(\mathcal{X}^{k+1} + \frac{\Lambda^k}{\mu}\right)\|_F^2. \quad (20)$$

Then, a flexible denoising CNN, *i.e.*, FFDNet [41], is utilized as a deep denoiser. Taking $\mathcal{X}^{k+1} + \Lambda^k/\mu$ as the input of FFDNet, the solution of Eq. (20) can be obtained as

$$\mathcal{Z}^{k+1} = \text{FFDNet}(\mathcal{X}^{k+1} + \frac{\Lambda^k}{\mu^k}, \beta), \quad (21)$$

where $\beta = \sqrt{\alpha/\mu}$. Under the PnP framework, $\mathcal{X}^{k+1} + \Lambda^k/\mu$ is taken as the noisy image, and the denoising result $\mathcal{Z}$ is obtained by the plugged prior.

Update Λ **and** μ: For the multiplier Λ, it is updated by

$$\Lambda^{k+1} = \Lambda^k + \mu^k(\mathcal{X}^{k+1} - \mathcal{Z}^{k+1}). \quad (22)$$

And the parameter μ can be updated by

$$\mu^{k+1} = \min\{\rho * \mu^k, \text{Max}\}, \quad (23)$$

where ρ denotes an adjustable parameters, and Max denotes the maximum value of the μ. Inspired by [49] and [32], the iterative regularization scheme is introduced, which is expressed as

$$\mathcal{A}^{k+1} = \mathcal{X}^k + \theta(\mathcal{A} - \mathcal{X}^k), \quad (24)$$

where k is the iteration number, and θ denotes the relaxation parameter. Finally, the whole algorithm procedure is summarized in Algorithm 2.

Algorithm 2 DLRQP for Color Image Denoising

Input: The noisy image $\mathcal{A} \in \mathbb{R}^{M\times N\times 3}$, the parameter μ, α, relaxation parameter θ, noise level τ.
Initialization: $\mathcal{X}^0 = \mathcal{Z}^0 = \mathcal{A}$, $\Lambda^0 = \text{zeros}(M \times N \times 3)$, $\mathcal{A}^0 = \mathcal{A}$, $\mu^0 = 0.001$, $\rho = 1.1$.
1: **for** $k = 0 : K$ **do**
2: Iterative regularization via Eq. (24);
3: **for** $\mathbf{a}_i$ in $\mathcal{A}^k$ **do**
4: Build similar patch group $\mathbf{A}_i$, $\mathbf{Z}_i$, Λ_i and convert
5: them to quaternion matrices $\dot{\mathbf{A}}_i$, $\dot{\mathbf{Z}}_i$, $\dot{\mathbf{R}}_i$;
6: Update $\dot{\mathbf{X}}_i$ via Eq. (15);
7: Convert $\dot{\mathbf{X}}_i$, $\dot{\mathbf{Z}}_i$, $\dot{\mathbf{R}}_i$ into real matrices $\mathbf{X}_i$, $\mathbf{Z}_i$, Λ_i;
8: **end for**
9: Aggregate $\{\mathbf{X}_i\}$, $\{\mathbf{Z}_i\}$, $\{\Lambda_i\}$ to construct the
10: complete images $\mathcal{X}^k$, $\mathcal{Z}^k$, and the multiplier Λ^k;
11: Update $\mathcal{Z}^{k+1}$ via Eq. (21);
12: Update Λ^{k+1} via Eq. (22);
13: Update μ^{k+1} via Eq. (23);
14: **end for**
Output: The denoised image $\mathcal{X}^k$.

C. DLRQP for Color Image Inpainting

As aforementioned, another classic image processing task is color image inpainting, whose aim is to reconstruct a complete image from observation with missing pixels. Adopting the proposed low-rank quaternion representation incorporated with deep image prior, our color image inpainting model is written as follows

$$\begin{aligned} &\min_{\dot{\mathbf{X}}} \quad \|\dot{\mathbf{X}}\|_{\gamma,\text{QNN}} + \lambda\Phi(\mathcal{X}), \\ &s.t. \quad \mathcal{P}_\Omega(\dot{\mathbf{X}}) = \mathcal{P}_\Omega(\mathcal{O}), \end{aligned} \quad (25)$$

where $\dot{\mathbf{X}} \in \mathbb{H}^{M\times N}$ indicates the reconstructed image, and $\dot{\mathbf{O}}$ denotes the incomplete observation. Ω denotes the index set of the observed elements. The operation $\mathcal{P}_\Omega(\cdot)$ denotes the projection function, which retains the elements in Ω consistent, while the rest be zeros. $\mathcal{X}$ is the tensor representation of the color image, and $\Phi(\mathcal{X})$ is an implicit regularizer to plug a deep denoiser. This model combines the superior global information construction capability of quaternion representation with the advantages of advanced deep denoisers for capturing local details. Due to missing pixels, the NSS property cannot be guaranteed. Thus, the low-rank restriction is imposed on the whole color image.

To facilitate computation, we introduce the auxiliary variable $\mathcal{Z} \in \mathbb{R}^{M\times N\times 3}$ and one auxiliary quaternion matrix variable $\dot{\mathbf{E}} \in \mathbb{H}^{M\times N}$, and the Eq. (25) is reformulated as

$$\begin{aligned} &\min_{\dot{\mathbf{X}},\dot{\mathbf{E}},\mathcal{Z}} \quad \|\dot{\mathbf{X}}\|_{\gamma,\text{QNN}} + \lambda\Phi(\mathcal{Z}), \\ &s.t. \quad \mathcal{Z} = \mathcal{X}, \quad \dot{\mathbf{X}} + \dot{\mathbf{E}} = \dot{\mathbf{O}}, \quad \mathcal{P}_\Omega(\dot{\mathbf{E}}) = \dot{\mathbf{0}}. \end{aligned} \quad (26)$$

The corresponding augmented Lagrangian function of the problem (26) is

$$\begin{aligned}&\mathcal{L}(\dot{\mathbf{X}}, \dot{\mathbf{E}}, \mathcal{Z}; \dot{\mathbf{M}}, \mathcal{Y})\\&= \|\dot{\mathbf{X}}\|_{\gamma,\mathrm{QNN}} + \lambda\Phi(\mathcal{Z})\\&\quad + \frac{\mu}{2}\|\dot{\mathbf{O}} - \dot{\mathbf{X}} - \dot{\mathbf{E}} + \frac{\dot{\mathbf{M}}}{\mu}\|_F^2 + \frac{\mu}{2}\|\mathcal{X} - \mathcal{Z} + \frac{\mathcal{Y}}{\mu}\|_F^2, \quad (27)\end{aligned}$$

where $\dot{\mathbf{M}}$ and $\mathcal{Y}$ indicates the Lagrangian multipliers. μ denotes a parameter. Then, an ADMM-based solution procedure is developed to solve the minimization problem under the PnP framework. We solve the above problem by update each variable alternately as follows:

$$\begin{aligned}\dot{\mathbf{X}}^{k+1} &= \arg\min_{\dot{\mathbf{X}}} \|\dot{\mathbf{X}}\|_{\gamma,\mathrm{QNN}} + \frac{\mu^k}{2}\|\dot{\mathbf{O}} - \dot{\mathbf{X}} - \dot{\mathbf{E}}^k + \frac{\dot{\mathbf{M}}^k}{\mu^k}\|_F^2\\&\quad + \frac{\mu}{2}\|\dot{\mathbf{X}} - \dot{\mathbf{Z}}^k + \frac{\dot{\mathbf{Y}}^k}{\mu^k}\|_F^2, \quad (28)\\\dot{\mathbf{E}}^{k+1} &= \arg\min_{\mathcal{P}_\Omega(\dot{\mathbf{E}})=\dot{\mathbf{0}}} \|\dot{\mathbf{O}} - \dot{\mathbf{X}}^{k+1} - \dot{\mathbf{E}} + \frac{\dot{\mathbf{M}}^k}{\mu^k}\|_F^2, \quad (29)\\\mathcal{Z}^{k+1} &= \arg\min_{\mathcal{Z}} \lambda\Phi(\mathcal{Z}) + \frac{\mu}{2}\|\mathcal{X} - \mathcal{Z} + \frac{\mathcal{Y}}{\mu}\|_F^2, \quad (30)\\\dot{\mathbf{M}}^{k+1} &= \dot{\mathbf{M}}^k + \mu^k(\dot{\mathbf{O}} - \dot{\mathbf{X}}^{k+1} - \dot{\mathbf{E}}^{k+1}), \quad (31)\\\mathcal{Y}^{k+1} &= \mathcal{Y}^k + \mu^k(\mathcal{X}^{k+1} - \mathcal{Z}^{k+1}), \quad (32)\\\mu^{k+1} &= \min\{\rho * \mu^k, \mathrm{Max}\}. \quad (33)\end{aligned}$$

Specifically, for the $\dot{\mathbf{X}}$ subproblem in (28), the preprocessing step here is to convert the tensors $\mathcal{X}$, $\mathcal{Z}$, and $\mathcal{A}$ into quaternion representations using the $\hbar$ operator. Then, the $\dot{\mathbf{X}}$ subproblem can be rewirten as

$$\begin{aligned}\dot{\mathbf{X}}^{k+1} &= \arg\min_{\dot{\mathbf{X}}} \|\dot{\mathbf{X}}\|_{\gamma,\mathrm{QNN}}\\&\quad + \mu\|\dot{\mathbf{X}} - \frac{\dot{\mathbf{O}} - \dot{\mathbf{E}}^k + \dot{\mathbf{M}}^k/\mu^k + \dot{\mathbf{Z}}^k - \dot{\mathbf{Y}}^k/\mu^k}{2}\|_F^2. \quad (34)\end{aligned}$$

The closed-form solution of Eq. (34) is obtained by Algorithm 1. The subproblem in (29) can be tackled by $\dot{\mathbf{O}} - \dot{\mathbf{X}}^{k+1} + \dot{\mathbf{M}}^k/\mu^k$. Meanwhile, we utilize the constraint $\mathcal{P}_\Omega(\dot{\mathbf{E}}) = \dot{\mathbf{0}}$ throughout the iteration to ensure that the observed pixels will not be changed. The $\mathcal{Z}$ subproblem in (30) can be solved by

$$\mathcal{Z}^{k+1} = \mathrm{FFDNet}(\mathcal{X}^{k+1} + \frac{\mathcal{Y}^k}{\mu^k}, \sqrt{\lambda/\mu^k}). \quad (35)$$

The details about the proposed DLRQP for color image inpainting are outlined in Algorithm 3.

D. Differences From Existing Methods

In this subsection, we aim to discuss the differences among our proposed approach and five closely related methods abbreviated as PNMM [12], SSLRDM [13], DSRDP [44], GLON [26] and DP3LRTC [27].

A common shortcoming of the PNNM and SSLRDM methods is that both of them use matrix to represent image data. The color image needs to be concatenated or sliced into matrix, and then input into the models. This way of processing three color channels separately will cause structure information loss. The CNN-based DSRDP method is inevitable to use a large number of images to train the model first. The tensor representation is used to reconstruct the tensor data in GLON and DP3LRTC. However, these approaches are not general enough to deal with color image denoising task.

Instead of tensor representation, our proposed DLRQP method integrates low-rank quaternion representation and deep prior into one unified framework without training for color image denoising and inpainting. Compared with matrix representation, the quaternion representation can process three color channels of the color image at the same time, which realizes the preservation of the inherent structural information of the color image. Compared with tensor representation, QR preserves the orthogonal character for the coefficients of three channels, which attains a structured representation [34]. Meanwhile, the low-rank quaternion and deep denoiser in the unified framework provide global and local priors to complement each other. Compared with only using traditional priors or deep priors, our proposed method can deal with complex scenarios more flexibly without pre-training. In short, the proposed DLRQP significantly differs from the above related methods.

Algorithm 3 DLRQP for Color Image Inpainting

Input: The observation $\mathcal{O}$, the indexes of observed pixels $\mathbf{\Omega}$, convergence criteria ξ.

Initialization: $\dot{\mathbf{X}}^{(0)} = \dot{\mathbf{E}}^{(0)} = \dot{\mathbf{M}}^{(0)} = \dot{\mathbf{0}}$, $\mathcal{Z}^{(0)} = \mathcal{O}$, $\mathcal{X}^{(0)} = \mathcal{Y}^{(0)} = 0$, $k = 0$, $\mu^0 = 0.001$, $\rho = 1.1$.

repeat
- $\dot{\mathbf{X}} = \hbar(\mathcal{X})$, $\dot{\mathbf{Z}} = \hbar(\mathcal{Z})$, $\dot{\mathbf{Y}} = \hbar(\mathcal{Y})$;
- Update $\dot{\mathbf{X}}^{k+1}$ by Eq. (34) (Algorithm 1);
- Update $\dot{\mathbf{E}}^{k+1}$ by Eq. (29);
- $\mathcal{X} = \hbar^{-1}(\dot{\mathbf{X}})$, $\mathcal{Z} = \hbar^{-1}(\dot{\mathbf{Z}})$, $\mathcal{Y} = \hbar^{-1}(\dot{\mathbf{Y}})$;
- Update $\mathcal{Z}^{k+1}$ by Eq. (35);
- Update $\dot{\mathbf{M}}^{k+1}$ by Eq. (31);
- Update $\mathcal{Y}^{k+1}$ by Eq. (32);
- Update μ^{k+1} by Eq. (33);

until $\frac{\|\dot{\mathbf{O}} - \dot{\mathbf{X}}^{k+1} - \dot{\mathbf{E}}^{k+1}\|_F^2}{\|\dot{\mathbf{O}}\|_F^2} \le \xi$

Output: The reconstructed tensor $\mathcal{X}$.

E. Computational Complexity

In this section, we discuss the computational complexity of the proposed DLRQP model. For color image denoising, the time for computing subproblem $\dot{\mathbf{X}}$ is mainly consumed by quaternion SVD, and the complexity is $O(p\min(n_1 n_2^2, n_1^2 n_2))$, where p denotes the number of patches; the complexity of computing subproblem $\mathcal{Z}$ is $O(n_1 n_2 n_l n_f n_k)$, where n_l, n_f, and n_k denotes the number of layers, features, and kernel pixels; the computational complexity of the multiplier Λ is $O(n_1 n_2)$. Thus, the total cost of DLRQP for color image denoising is $O(p\min(n_1 n_2^2, n_1^2 n_2) + n_1 n_2 n_l n_f n_k + n_1 n_2)$. Analogously, the

TABLE II
DENOISING ASSESSMENT (PSNR/SSIM) OF THE PROPOSED AND COMPETING METHODS

Methods	LSCD	KQSVD	WNNM	LRQA	FFDNet	TLRSR	GSHOSVD	Our
Images:	$\tau = 10$							
Img1	34.47/0.934	33.81/0.927	34.66/0.938	34.77/0.941	35.59/0.953	30.98/0.938	30.68/0.871	**35.87/0.955**
Img2	28.79/0.870	28.47/0.877	30.45/0.907	30.48/0.908	31.06/0.923	27.20/0.857	27.97/0.861	**31.16/0.925**
Img3	32.73/0.906	32.78/0.913	34.78/0.945	34.99/0.948	36.04/0.955	33.55/0.953	31.73/0.878	**36.19/0.958**
Img4	31.08/0.922	30.90/0.918	32.95/0.940	33.11/0.944	34.11/0.957	**36.04/0.977**	29.69/0.912	34.20/0.958
Img5	33.97/0.862	34.20/0.846	35.75/0.897	**36.03/0.907**	34.66/0.899	32.48/0.920	31.67/0.839	35.01/0.906
Img6	34.73/0.928	34.20/0.922	35.23/0.934	35.41/0.939	36.72/0.949	32.06/0.939	31.22/0.876	**36.77/0.950**
Img7	33.16/0.944	33.12/0.942	34.67/0.958	34.75/0.959	36.18/0.967	31.04/0.950	30.80/0.913	**36.31/0.968**
Img8	31.98/0.916	31.88/0.916	32.77/0.922	32.76/0.925	33.21/0.935	28.41/0.906	29.86/0.890	**33.34/0.937**
Img9	33.47/0.877	33.61/0.884	34.05/0.888	34.16/0.891	35.29/0.913	31.60/0.899	30.40/0.860	**35.38/0.918**
Img10	33.76/0.974	32.56/0.965	35.05/0.984	34.96/0.984	36.02/0.988	30.46/0.959	28.79/0.944	**36.09/0.988**
Img11	34.24/0.940	33.34/0.931	34.37/0.943	34.57/0.947	36.74/0.966	32.39/0.953	30.91/0.894	**36.76/0.966**
Img12	32.60/0.929	31.11/0.917	33.93/0.940	34.02/0.943	35.02/0.955	26.79/0.901	29.86/0.883	**35.08/0.957**
Aver.	32.915	32.498	34.055	34.168	35.053	31.083	30.298	**35.180**
Images:	$\tau = 30$							
Img1	28.33/0.813	28.67/0.845	28.97/0.857	29.27/0.867	30.55/0.901	25.26/0.785	25.14/0.681	**30.87/0.903**
Img2	24.13/0.663	24.17/0.673	24.47/0.679	24.80/0.712	25.93/0.780	22.25/0.616	23.65/0.629	**26.02/0.787**
Img3	27.88/0.792	27.91/0.799	28.91/0.836	29.40/0.854	30.62/0.878	26.18/0.774	26.41/0.705	**30.70/0.883**
Img4	25.92/0.774	25.83/0.748	26.94/0.793	27.51/0.824	28.64/0.865	**30.26/0.923**	24.82/0.749	28.75/0.871
Img5	29.77/0.772	29.83/0.787	31.91/0.818	**32.18**/0.826	31.44/0.827	26.86/0.790	26.64/0.635	31.91/**0.831**
Img6	29.40/0.831	29.19/0.825	29.76/0.848	30.16/0.859	31.67/0.893	25.80/0.764	25.96/0.696	**31.75/0.896**
Img7	27.78/0.854	27.70/0.859	28.71/0.888	29.01/0.895	30.47/0.923	22.86/0.693	25.71/0.767	**30.66/0.926**
Img8	26.73/0.796	26.95/0.810	26.93/0.813	27.05/0.823	28.28/0.863	23.17/0.710	25.06/0.722	**28.47/0.866**
Img9	28.83/0.739	28.90/0.743	29.15/0.761	29.35/0.770	30.55/0.810	25.33/0.635	25.54/0.644	**30.62/0.818**
Img10	27.61/0.913	26.83/0.911	28.45/0.943	28.63/0.946	30.46/0.965	20.75/0.703	24.42/0.835	**30.58/0.967**
Img11	28.51/0.830	27.95/0.809	28.32/0.831	28.82/0.848	30.81/0.899	24.99/0.756	25.74/0.719	**30.85/0.903**
Img12	27.41/0.824	26.70/0.811	28.08/0.847	28.29/0.855	30.04/0.895	21.79/0.665	25.13/0.712	**30.07/0.898**
Aver.	27.692	27.553	28.383	28.706	29.955	24.625	25.352	**30.104**
Images:	$\tau = 50$							
Img1	21.57/0.391	25.96/0.773	26.56/0.801	26.89/0.813	28.22/0.865	17.63/0.245	22.21/0.504	**28.27/0.867**
Img2	20.49/0.437	22.39/0.511	22.61/0.532	22.93/0.573	23.87/0.658	17.48/0.308	21.54/0.493	**23.92/0.678**
Img3	21.83/0.462	25.50/0.712	26.40/0.762	26.89/0.781	28.33/0.823	18.98/0.351	24.07/0.619	**28.39/0.828**
Img4	20.95/0.517	23.44/0.592	24.30/0.660	24.94/0.710	26.24/0.779	24.67/0.771	22.68/0.646	**26.27/0.783**
Img5	23.00/0.402	27.32/0.732	29.95/0.789	**30.26**/0.794	29.88/0.806	19.91/0.315	24.27/0.554	30.25/**0.809**
Img6	22.82/0.462	26.63/0.748	27.44/0.788	27.90/0.802	29.31/0.848	18.61/0.288	23.39/0.605	**29.39/0.851**
Img7	21.62/0.539	25.06/0.784	26.09/0.831	26.42/0.837	27.92/0.884	16.06/0.290	23.16/0.692	**28.16/0.889**
Img8	21.28/0.459	24.49/0.723	24.62/0.739	24.76/0.750	25.99/0.807	17.12/0.287	22.66/0.631	**26.07/0.810**
Img9	22.99/0.397	26.63/0.653	27.04/0.688	27.25/0.695	28.31/0.745	15.33/0.136	22.60/0.496	**28.37/0.752**
Img10	21.05/0.680	23.87/0.854	25.32/0.900	25.64/0.905	27.65/0.941	13.19/0.341	21.54/0.766	**27.86/0.944**
Img11	22.27/0.495	25.23/0.701	25.84/0.746	26.39/0.770	28.10/**0.935**	19.26/0.361	23.37/0.615	**28.14**/0.839
Img12	21.86/0.503	24.54/0.733	25.31/0.778	25.60/0.785	27.70/**0.848**	15.53/0.240	22.83/0.612	**27.77/0.848**
Aver.	21.811	25.088	25.957	26.323	27.626	16.981	22.860	**27.738**

main computational cost of DLRQP for color image inpainting is $O(\min(n_1 n_2^2, n_1^2 n_2) + n_1 n_2 n_l n_f n_k + n_1 n_2)$.

However, the convergence proof of the framework incorporating deep denoisers is still an open issue. But the effectiveness and superiority of deep denoisers are remarkable, which should be explored more deeply and extensively by more researchers [26]. More recently, Ryu et al. theoretically established the convergence of PnP-ADMM and proposed that the PnP-ADMM would converge to a fixed point if the deep learning denoiser is properly trained [61]. Thus, the theoretical proof is beyond the research focus of this work.

IV. EXPERIMENTAL RESULTS AND ANALYSIS

To illustrate the superiority of the proposed DLRQP model, we carry out several experiments on two typical color image processing tasks: color image denoising and inpainting. We implement all experiments on the platform of Windows 10 running on a desktop with an Intel(R) Core (TM) i9-10900 CPU at 3.70GHz and 64GB RAM.

A. Quantitative Assessment

The performance of the DLRQP is quantitatively evaluated by two evaluation indicators, *i.e.*, peak signal-to-noise ratio (PSNR), and structural similarity index (SSIM) [62].

In general, the larger the values of PSNR and SSIM, the better the performance of the algorithm.

B. Artificial Noisy Color Image Denoising

1) Color Image Data: The proposed algorithm is first evaluated on 12 natural RGB color images with the resolution of 256 × 256 as shown in Fig. 2, all of which are added with the additive Gaussian noise with mean zero and variance τ^2 as simulated noise. Here we test the case where the noise levels τ are equal to 10, 30, and 50, respectively.

2) Compared Methods: We compare our proposed DLRQP with the following seven denoising methods, including LSCD [63], KQSVD [34], WNNM [64], LRQA [5], FFDNet [41], TLRSR [65], GSHOSVD [66]. Specifically, KQSVD and LRQA are both quaternion-based denoising methods, where LRQA represents weighted Schatten norm-based LRQA methods with the best denoising perfor-

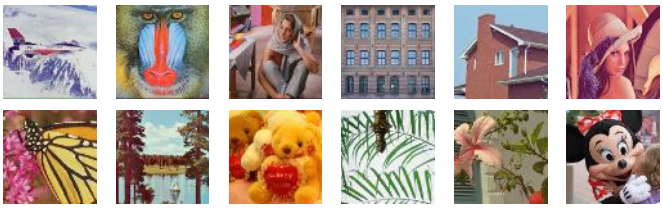

Fig. 2. The 12 RGB color images used in our denoising experiment. The images are named Img1 to Img12 from left to right.

mance in [5]. LSCD and WNNM are LRMA-based denoising methods. FFDNet is the deep learning-based method. TLRSR and GSHOSVD are tensor-based denoising methods.

3) Parameter Settings: For all comparison methods, we use the recommended parameter settings. In our proposed Algorithm 2, parameters that need to be considered include the patch size p, the number of similar patch groups m, the number of iterations K, and the iterative relaxation coefficient θ. In the case of τ=10, 30, 50, p is set to 6×6, 7×7, 8×8, and we set m to 70, 90, and 120, respectively. K and θ are fixed at 4 and 0.1, respectively.

Table II summarizes the PSNR and SSIM values of different denoising approaches under different noise levels. We use bold font to emphasize the best results and underline the second-best ones. Moreover, we calculate the average PSNR values for all methods at different noise levels. Some of experimental results in the Table II are quoted from [5]. It can be observed that our proposed DLRQP acquires the optimal performance in most cases. DLRQP has achieved 0.127dB, 0.149dB, and 0.112dB improvement over the runner-up FFDNet with respect to $\tau = 10$, 30, 50, respectively. This directly demonstrates the advantage of the proposed DLRQP for color image denoising. It can be found that FFDNet outperforms most traditional denoising methods. The reason is that FFDNet has powerful representation learning ability due to its complex network structure. The tensor-based methods TLRSR and GSHOSVD cannot outperform the quaternion-based method, we guess because tensor-based methods do not exploit nonlocal information. Besides, compared with the other two quaternion-based denoising methods, our method improves the average PSNR value about 2dB over KQSVD and about 1dB over LRQA. The above observation confirms the effectiveness of our proposed DLRQP. The main reason is that we adopt the quaternion representation and build a framework for unifying local, non-local, and global information, which improves the denoising performance.

Moreover, the visual results of color image denoising for all methods at noise level $\tau = 50$ are shown in Fig. 3. From the enlarged regions, we can observe that there is still obvious unexpected noise in the recovered images by LSCD, TLRSR and GSHOSVD. WNNM and LRQA denoise better, but still lose some details and textures. Compared with FFDNet, our method recovers more details in some regions with low pixel values and obtains higher PSNR values. In terms of visual effects, the proposed DLRQP outperforms other competing methods.

Fig. 3. Denoising results of all methods on the images "Sailboat" and "Bear" with $\tau = 50$.

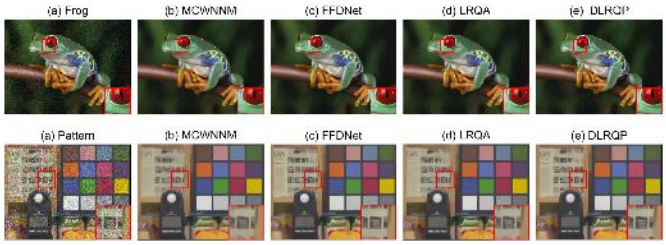

Fig. 4. Denoising results on real-world noisy images "Frog" and "Pattern".

C. Real Noisy Color Image Denoising

We evaluate the proposed DLRQP on real images for the denoising task. We selected two images from real-world noisy dataset RNI15 [67], namely Frog and Pattern. We compare the proposed DLRQP method with MCWNNM [32], FFDNet [41], LRQA [5]. We need to estimate the noise level on the real image first. Here we adopt the noise estimation method in [68] for each color channel. According to the best settings given in the FFDNet, we set the input noise to 15 for Frog and 40 for Pattern, respectively. For MCWNNM and LRQA, we set the patch size p is set to 6, the number of nonlocal similar patches m is set to 70, and the searching window is set to 20×20.

Since the ground truth cannot be obtained for real noisy images experiments, we only report the comparison of visual restoration results in Fig. 4. It can be observed that all methods recover clean images. However, the images denoised by MCWNNM and LRQA still exist some blur and noise, while the denoising results of our proposed method are clearer than that of other methods. Meanwhile, our method has fewer staircase artifacts on details than FFDNet.

D. Color Image Inpainting

In this section, we conduct color image inpainting experiments to evaluate the performance of the proposed DLRQP.

TABLE III
INPAINTING ASSESSMENT (PSNR/SSIM) OF THE PROPOSED AND COMPETING METHODS

Methods	LMaFit	TNNR	WNNM	MC-NC	D-N	LRQA	LRQMC	PnP-DIP	Our
Images:	MR = 0.50								
Img1	21.33/0.779	33.49/0.921	31.54/0.875	32.71/0.908	27.33/0.799	33.50/0.922	33.32/0.915	33.17/0.911	**34.99/0.953**
Img2	20.24/0.443	24.46/0.655	22.06/0.510	23.78/0.603	21.06/0.406	24.95/0.692	25.35/0.732	26.95/0.759	**27.92/0.884**
Img3	22.14/0.644	27.53/0.810	25.02/0.707	27.65/0.820	23.09/0.526	27.58/0.810	27.70/0.822	28.53/0.851	**29.94/0.910**
Img4	23.17/0.558	26.62/0.708	25.24/0.636	26.86/0.723	24.14/0.490	27.88/0.769	28.18/0.789	28.54/0.803	**31.01/0.894**
Img5	24.07/0.941	28.42/0.966	26.96/0.948	28.63/0.967	21.40/0.864	29.03/0.969	29.30/0.971	27.43/0.956	**31.88/0.984**
Img6	21.95/0.775	27.65/0.887	24.92/0.805	27.94/0.898	24.82/0.750	27.85/0.885	28.21/0.899	**29.60/0.919**	29.38/0.918
Img7	28.01/0.864	36.61/0.956	33.96/0.905	36.20/0.950	30.63/0.814	36.60/0.958	35.39/0.940	33.15/0.903	**39.03/0.976**
Img8	18.67/0.700	24.27/0.840	21.32/0.748	24.16/0.837	19.71/0.610	24.48/0.845	24.49/0.847	**27.92/0.941**	27.22/0.933
Img9	16.01/0.377	29.00/0.823	28.24/0.790	28.16/0.788	15.42/0.372	30.17/0.845	28.86/0.821	25.77/0.678	**36.29/0.953**
Img10	23.71/0.597	29.55/0.810	27.38/0.703	29.66/0.816	21.08/0.391	29.71/0.811	29.75/0.825	30.11/0.855	**35.33/0.947**
Img11	22.13/0.655	34.85/0.913	33.28/0.867	33.82/0.881	20.79/0.554	35.66/0.920	35.23/0.919	32.76/0.819	**38.86/0.956**
Img12	22.36/0.374	29.55/0.810	26.62/0.683	19.26/0.418	12.61/0.296	28.39/0.734	27.99/0.760	31.96/0.852	**34.21/0.949**
Aver.	21.332	30.316	27.209	27.878	21.840	30.583	29.481	29.658	**33.005**
Images:	MR = 0.75								
Img1	17.05/0.424	28.30/0.789	27.00/0.681	28.52/0.791	26.44/0.735	28.64/0.799	28.40/0.797	30.64/0.859	**32.12/0.926**
Img2	13.94/0.139	19.99/0.362	18.19/0.250	18.53/0.265	20.11/0.330	21.41/0.444	21.38/0.484	**24.60/0.745**	24.14/0.743
Img3	15.76/0.219	23.06/0.562	21.09/0.404	22.70/0.521	22.27/0.467	23.72/0.578	23.66/0.597	26.65/0.802	**26.70/0.806**
Img4	16.96/0.190	22.88/0.461	21.43/0.351	23.10/0.448	23.42/0.436	24.53/0.547	24.61/0.574	26.96/0.712	**27.54/0.765**
Img5	15.55/0.674	23.05/0.894	21.26/0.843	23.30/0.900	20.57/0.837	23.57/0.901	22.84/0.896	22.84/0.863	**26.99/0.959**
Img6	17.27/0.541	23.78/0.770	21.91/0.662	23.77/0.748	23.89/0.719	24.68/0.781	25.10/0.796	25.52/0.809	**26.49/0.840**
Img7	19.28/0.497	30.08/0.848	28.78/0.744	31.19/0.856	29.37/0.782	31.78/0.877	30.60/0.856	30.32/0.847	**34.97/0.949**
Img8	14.11/0.446	19.45/0.647	17.52/0.563	19.00/0.585	18.65/0.541	20.50/0.666	20.43/0.672	**23.50/0.856**	23.41/0.851
Img9	14.13/0.223	22.48/0.528	20.96/0.467	19.54/0.324	15.28/0.311	23.61/0.554	22.63/0.538	21.47/0.516	**31.83/0.907**
Img10	19.97/0.450	25.06/0.584	22.93/0.495	23.73/0.504	20.90/0.487	25.38/0.580	25.56/0.629	26.56/0.688	**30.75/0.867**
Img11	18.90/0.493	29.34/0.760	27.36/0.744	28.53/0.689	20.69/0.513	30.20/0.774	28.95/0.757	29.11/0.823	**35.67/0.994**
Img12	11.70/0.120	21.91/0.463	20.56/0.413	15.53/0.129	12.46/0.089	22.75/0.428	21.38/0.421	24.99/0.634	**30.45/0.906**
Aver.	16.218	24.115	22.416	22.219	21.171	25.347	24.628	26.097	**29.255**
Images:	MR = 0.85								
Img1	11.24/0.043	24.52/0.619	23.72/0.495	20.83/0.312	24.83/0.648	26.14/0.683	24.22/0.662	28.92/0.858	**30.23/0.903**
Img2	11.22/0.077	16.81/0.181	16.31/0.137	15.96/0.146	19.01/0.246	19.90/0.322	19.83/0.367	**23.48/0.711**	23.02/0.666
Img3	10.91/0.085	20.07/0.363	18.81/0.245	18.03/0.226	21.09/0.383	22.03/0.449	21.82/0.463	25.32/0.729	**25.45/0.747**
Img4	12.67/0.079	20.31/0.285	19.72/0.228	19.54/0.224	22.26/0.363	23.08/0.429	23.10/0.464	25.86/0.653	**25.94/0.671**
Img5	10.08/0.301	18.97/0.777	16.43/0.653	16.69/0.671	19.28/0.789	20.42/0.824	19.10/0.795	19.25/0.806	**24.08/0.922**
Img6	12.85/0.263	21.17/0.652	20.14/0.570	19.30/0.537	22.66/0.674	23.34/0.714	23.36/0.729	22.99/0.687	**25.21/0.776**
Img7	15.21/0.193	26.32/0.694	26.19/0.603	24.54/0.546	27.77/0.733	29.75/0.803	27.76/0.776	29.51/0.799	**32.94/0.922**
Img8	10.41/0.079	16.63/0.491	15.66/0.443	15.69/0.190	17.43/0.459	18.77/0.539	18.87/0.557	**21.92**/0.784	21.70/**0.801**
Img9	13.97/0.181	18.94/0.333	16.83/0.189	13.44/0.096	15.15/0.248	18.67/0.272	18.06/0.313	19.27/0.411	**28.15/0.851**
Img10	19.78/0.406	22.72/0.456	20.26/0.249	18.53/0.229	20.48/0.424	22.89/0.423	22.78/0.495	27.56/0.753	**28.34/0.790**
Img11	18.81/0.447	26.42/0.626	23.81/0.424	20.43/0.214	20.52/0.526	26.61/0.932	23.81/0.521	26.37/0.734	**29.23/0.844**
Img12	11.56/0.090	18.93/0.313	16.95/0.144	12.20/0.060	12.34/0.165	18.77/0.230	16.83/0.202	21.34/0.556	**27.56/0.868**
Aver.	13.226	20.984	19.569	16.684	20.235	21.974	21.628	24.316	**26.763**

Fig. 5. The 12 RGB color images used in our inpainting experiment. The images are named Img1 to Img12 from left to right.

The selected 12 color images are shown in Fig 5. The image inpainting methods chosen for comparison include LRMA-based LMaFit [69], TNNR [8], WNNM [49], MC-NC [70], D-N [71], quaternion-based LRQA [5], LRQMC [33], and plug-and-play-based PnP-DIP [72]. Among them, LRQA in [5] represents the LRQA model using the Laplace function, which achieves relatively optimal performance in the color image inpainting task.

Quantitative evaluations of inpainting performance from all methods are presented in Table III. We test three missing rate (MR) cases, namely MR = 0.5, 0.75, 0.85. It is observed that the proposed DLRQP achieves the best performance in most cases. Compared with the quaternion-based inpainting methods LRQA and LRQMC, DLRQP improves the average PSNR at least 2.5dB since DLRQP also takes the deep prior of color images into consideration. In addition, we find that the performance of the LRMA-based method MC-NC drops sharply as the missing rate increases. In contrast, the proposed DLRQP has better stability. Driven by the powerful structure retention of quaternion representation, DLRQP has surpassed the PnP-based color image inpainting method PnP-DIP, by a large margin. The corresponding improvement is at least 2.6dB. It is worth noting that the improvement of DLRQP on color image inpainting is much obvious than that on color image denoising. We attribute this to the use of nonlocal self-similarity, which may bring the loss of some structural information of color images.

Fig. 6 shows the comparison of visual effects of all methods with MR = 0.85. As we can see, LMaFit and D-N have poor recovery performance at high missing rates. TNNR, WNNM, MC-NC, and LRQMC recover rough structures, but the images still exist obvious missing pixels. LRQA and PnP-DIP

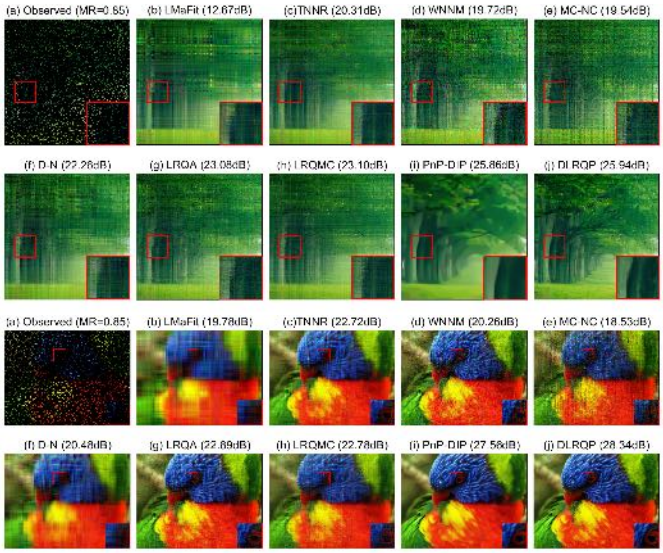

Fig. 6. Inpainting visual effects of all methods on the Img4 and Img10 with MR = 0.85.

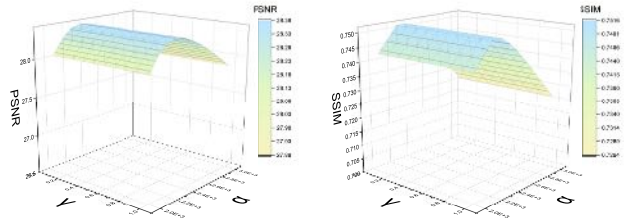

Fig. 7. PSNR and SSIM values of DLRQP with respect to γ and α on Img9 for color image denoising.

recover better results, but also have some loss of details. The results of PnP-DIP are over-smooth. In comparison, the proposed DLRQP achieves the most visually desirable results with pleasing image details and neat textures. This also confirms the effectiveness of the proposed model combining nonconvex low-rank approximation and FFDNet denoiser in the quaternion domain.

E. Discussion

1) Parameter Selection: We test the influence of the parameters γ and α in our proposed DLRQP. In the proposed model, γ and α control the weights of the low-rank prior and deep prior, respectively. If γ is not suitable for the proposed model, it will affect the integrality of the restored image. If α is too large or too small, it will compromise the local smoothness and details of the image. Based on this, we conduct related experiments on color image denoising with $\tau = 50$. We set γ to [0.1, 1] with an increment of 0.1, and set α from 2E+3 to 3E+3 with an increment of 1E+2. Fig. 7 shows the effect of different γ and α on PSNR and SSIM for color image denoising. It can be found that the adjustment of parameter α has a greater impact on the results. Satisfactory experimental results can be obtained when $\alpha = [2.4\text{E}{+}3, 2.6\text{E}{+}3]$ for color image denoising. Our DLRQP is insensitive to parameter γ, which shows the robustness of the nonconvex low-rank prior.

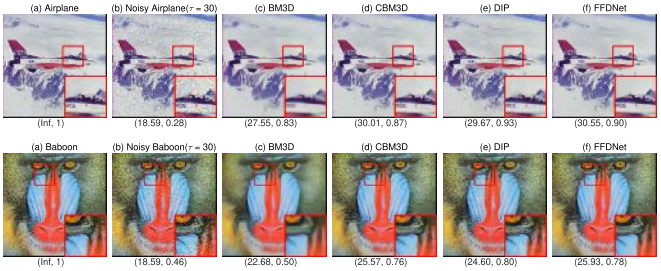

Fig. 8. The denoising performance of BM3D [73], CBM3D [74], DIP [75], and FFDNet [41] on images "Airplane" and "Baboon" with noise level $\tau = 30$. The values below each image are the corresponding PSNR and SSIM.

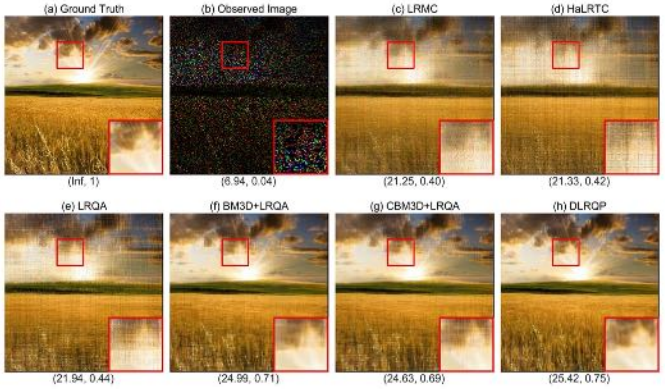

Fig. 9. The inpainting performance of LRMC [48], HaLRTC [24], LRQA [5], LRQA+BM3D, LRQA+CBM3D, and DLRQP on two images with MR = 0.85. The values below each image are the corresponding PSNR and SSIM.

2) Choice of Denoiser for DLRQP: To investigate the effect of different denoisers for our method, we compare the denoising performance of BM3D [73], CBM3D [74], DIP [75], and FFDNet [41] on two images with noise level $\tau = 30$. Visual and numerical results are shown in Fig. 8. We can see that the images recovered by BM3D are over smooth, and CBM3D and DIP methods suffer from blurring in details. Note that the SSIM values of DIP is higher than that of FFDNet. We attribute this to that the particular generator network structure in DIP is beneficial to the reconstruction of the structural information of the image. FFDNet can retain more details, and whose PSNR is also higher than that of other methods, which verifies the advantages of the used FFDNet in improving the image restoration performance.

3) Ablation Experiments: To illustrate the effectiveness of the different terms of the proposed method, we discuss the contributions of low-rank quaternion prior and FFDNet for color image inpainting with the MR=0.85 in Fig. 9. It can be seen that the matrix-based LRMC [48] and the Tucker-based HaLRTC [24] are slightly inferior to the quaternion-based LRQA [5]. Besides, compared with LRQA, the inpainting performance combined with the plug-and-play denoiser is significantly improved. The proposed DLRQP outperforms BM3D+LRQA and CBM3D+LRQA and is closer to the ground truth. As a whole, we can conclude that the unified framework of quaternion combined with deep denoiser prior is effective, and the FFDNet we utilized in the framework can achieve promising performance.

TABLE IV
AVERAGE RUNNING TIME (IN SECONDS) OF THE PROPOSED AND COMPETING METHODS

Color Image Denoising				
LSCD	KQSVD	WNNM	LRQA	
3.37	7.24	433.35	379.39	
FFDNet	TLRSR	GSHOSVD	DLRQP	
0.0058	1.16	4989.63	171.62	
Color Image Inpainting				
LMaFit	TNNR	WNNM	MC-NC	D-N
0.32	105.12	320.16	27.72	7.12
LRQA	LRQMC	PnP-DIP	DLRQP	
134.86	52.91	5526.59	35.74	

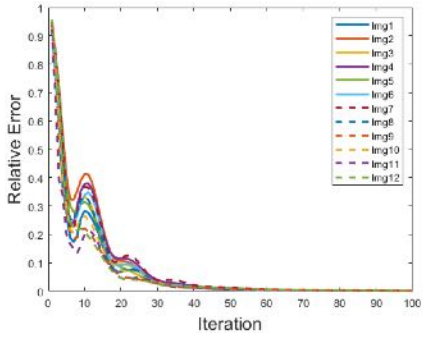

Fig. 10. The convergence curves about relative error and iterations on Img1-Img12.

4) Running Time: We further report the average running time of all approaches on all images for color image denoising and inpainting as shown in Table IV. For color image inpainting, LMaFit has the shortest running time since it is based on matrix factorization without computationally time-consuming SVD. For color image denoising, the shortest time-consuming method is FFDNet, because FFDNet has been pre-trained and uses GPU-accelerated operations. Overall, the runtime of the proposed is comparable.

5) Convergence Behaviors: Fig. 10 illustrates the numerical convergence of our algorithm under MR $= 0.85$ on all images. It can be seen that the relative error decreases as the number of iterations increasing. During the period, the proposed DLRQP method has some fluctuations in the curve at the beginning of the iteration. The reason for the fluctuations may be that the deep denoiser incorporated in the proposed framework makes the solution of model unstable. Ultimately, the model still tends to converge.

V. CONCLUSION

In this paper, we exploited the complementary advantages of deep plug-and-play prior and quaternion representation and proposed a novel color image processing model, termed as plug-and-play prior regularized low-rank quaternion representation. Unlike existing matrix-based and tensor-based methods, our DLRQP model was not only able to process three channels simultaneously and holistically by the quaternion representation, but also preserved the structural features of color images by pursuing the deep prior. Under the leverage of plugged deep denoiser, more image details could be preserved. Then, we applied the proposed DLRQP model to solve two color image processing applications, *i.e.*, color image denoising and color image inpainting, and proposed optimization procedures, respectively. The results of numerical experiments illustrated the superiority of the proposed DLRQP model compared to other competing methods. The potential research direction is how to extend the proposed DLRQP into other color image tasks, such as color image deblurring, color image recognition, color image super-resolution and so on.

REFERENCES

[1] C. Zou, K. Kou, and Y. Wang, "Quaternion collaborative and sparse representation with application to color face recognition," *IEEE Trans. Image Process.*, vol. 25, no. 7, pp. 3287–3302, Jul. 2016.
[2] Z. Hua, Z. Zhu, Y. Chen, and Y. Li, "Color image encryption using orthogonal Latin squares and a new 2D chaotic system," *Nonlinear Dyn.*, vol. 104, no. 4, pp. 4505–4522, Jun. 2021.
[3] S. Gai and X. Huang, "Reduced biquaternion convolutional neural network for color image processing," *IEEE Trans. Circuits Syst. Video Technol.*, vol. 32, no. 3, pp. 1061–1075, Mar. 2022.
[4] Z. Zha, X. Yuan, B. Wen, J. Zhou, J. Zhang, and C. Zhu, "A benchmark for sparse coding: When group sparsity meets rank minimization," *IEEE Trans. Image Process.*, vol. 29, pp. 5094–5109, 2020.
[5] Y. Chen, X. Xiao, and Y. Zhou, "Low-rank quaternion approximation for color image processing," *IEEE Trans. Image Process.*, vol. 29, pp. 1426–1439, 2020.
[6] Z. Zha, B. Wen, X. Yuan, J. Zhou, C. Zhu, and A. C. Kot, "A hybrid structural sparsification error model for image restoration," *IEEE Trans. Neural Netw. Learn. Syst.*, vol. 33, no. 9, pp. 4451–4465, Sep. 2022.
[7] Z. Zha, B. Wen, X. Yuan, J. Zhou, and C. Zhu, "Image restoration via reconciliation of group sparsity and low-rank models," *IEEE Trans. Image Process.*, vol. 30, pp. 5223–5238, 2021.
[8] Y. Hu, D. Zhang, J. Ye, X. Li, and X. He, "Fast and accurate matrix completion via truncated nuclear norm regularization," *IEEE Trans. Pattern Anal. Mach. Intell.*, vol. 35, no. 9, pp. 2117–2130, Sep. 2013.
[9] W. Ren, X. Cao, J. Pan, X. Guo, W. Zuo, and M.-H. Yang, "Image deblurring via enhanced low-rank prior," *IEEE Trans. Image Process.*, vol. 25, no. 7, pp. 3426–3437, Jul. 2016.
[10] H. Zhang, J. Qian, B. Zhang, J. Yang, C. Gong, and Y. Wei, "Low-rank matrix recovery via modified schatten-p norm minimization with convergence guarantees," *IEEE Trans. Image Process.*, vol. 29, pp. 3132–3142, 2019.
[11] Y. Chen, Y. Guo, Y. Wang, D. Wang, C. Peng, and G. He, "Denoising of hyperspectral images using nonconvex low rank matrix approximation," *IEEE Trans. Geosci. Remote Sens.*, vol. 55, no. 9, pp. 5366–5380, Sep. 2017.
[12] X. Zhang, J. Zheng, D. Wang, and L. Zhao, "Exemplar-based denoising: A unified low-rank recovery framework," *IEEE Trans. Circuits Syst. Video Technol.*, vol. 30, no. 8, pp. 2538–2549, Aug. 2020.
[13] H. Wang, Y. Li, Y. Cen, and Z. He, "Multi-matrices low-rank decomposition with structural smoothness for image denoising," *IEEE Trans. Circuits Syst. Video Technol.*, vol. 30, no. 2, pp. 349–361, Feb. 2020.
[14] H. Zhang, C. Gong, J. Qian, B. Zhang, C. Xu, and J. Yang, "Efficient recovery of low-rank matrix via double nonconvex nonsmooth rank minimization," *IEEE Trans. Neural Netw. Learn. Syst.*, vol. 30, no. 10, pp. 2916–2925, Oct. 2019.
[15] Q. Wang, X. Zhang, Y. Wu, L. Tang, and Z. Zha, "Nonconvex weighted ℓ_p minimization based group sparse representation framework for image denoising," *IEEE Signal Process. Lett.*, vol. 24, no. 11, pp. 1686–1690, Nov. 2017.
[16] Z. Zha, X. Yuan, B. Wen, J. Zhou, J. Zhang, and C. Zhu, "From rank estimation to rank approximation: Rank residual constraint for image restoration," *IEEE Trans. Image Process.*, vol. 29, pp. 3254–3269, 2020.
[17] P. Zhou, C. Lu, Z. Lin, and C. Zhang, "Tensor factorization for low-rank tensor completion," *IEEE Trans. Image Process.*, vol. 27, no. 3, pp. 1152–1163, Mar. 2018.
[18] C. Lu, J. Feng, Y. Chen, W. Liu, Z. Lin, and S. Yan, "Tensor robust principal component analysis with a new tensor nuclear norm," *IEEE Trans. Pattern Anal. Mach. Intell.*, vol. 42, no. 4, pp. 925–938, Jan. 2020.
[19] T.-X. Jiang, M. K. Ng, X.-L. Zhao, and T.-Z. Huang, "Framelet representation of tensor nuclear norm for third-order tensor completion," *IEEE Trans. Image Process.*, vol. 29, pp. 7233–7244, 2020.
[20] Y. Chen, S. Wang, C. Peng, Z. Hua, and Y. Zhou, "Generalized nonconvex low-rank tensor approximation for multi-view subspace clustering," *IEEE Trans. Image Process.*, vol. 30, pp. 4022–4035, 2021.

[21] J. A. Bengua, H. N. Phien, H. D. Tuan, and M. N. Do, "Efficient tensor completion for color image and video recovery: Low-rank tensor train," *IEEE Trans. Image Process.*, vol. 26, no. 5, pp. 2466–2479, May 2017.
[22] W. Wang, V. Aggarwal, and S. Aeron, "Efficient low rank tensor ring completion," in *Proc. IEEE Int. Conf. Comput. Vis. (ICCV)*, Oct. 2017, pp. 5697–5705.
[23] Q. Zhao, L. Zhang, and A. Cichocki, "Bayesian CP factorization of incomplete tensors with automatic rank determination," *IEEE Trans. Pattern Anal. Mach. Intell.*, vol. 37, no. 9, pp. 1751–1763, Sep. 2015.
[24] J. Liu, P. Musialski, P. Wonka, and J. Ye, "Tensor completion for estimating missing values in visual data," *IEEE Trans. Pattern Anal. Mach. Intell.*, vol. 35, no. 1, pp. 208–220, Jan. 2013.
[25] I. V. Oseledets, "Tensor-train decomposition," *SIAM J. Sci. Comput.*, vol. 33, no. 5, pp. 2295–2317, Jan. 2011.
[26] X.-L. Zhao, J.-H. Yang, T.-H. Ma, T.-X. Jiang, M. K. Ng, and T.-Z. Huang, "Tensor completion via complementary global, local, and nonlocal priors," *IEEE Trans. Image Process.*, vol. 31, pp. 984–999, 2022.
[27] X.-L. Zhao, W.-H. Xu, T.-X. Jiang, Y. Wang, and M. K. Ng, "Deep plug-and-play prior for low-rank tensor completion," *Neurocomputing*, vol. 400, pp. 137–149, Dec. 2020.
[28] F. Wu, Y. Li, C. Li, and Y. Wu, "A fast tensor completion method based on tensor QR decomposition and tensor nuclear norm minimization," *IEEE Trans. Comput. Imag.*, vol. 7, pp. 1267–1277, 2021.
[29] C. J. Hillar and L.-H. Lim, "Most tensor problems are NP-hard," *J. ACM*, vol. 60, no. 6, pp. 1–39, Nov. 2013.
[30] B. Chen et al., "Quaternion Zernike moments and their invariants for color image analysis and object recognition," *Signal Process.*, vol. 92, no. 2, pp. 308–318, 2012.
[31] S.-C. Pei and C.-M. Cheng, "A novel block truncation coding of color images using a quaternion-moment-preserving principle," *IEEE Trans. Commun.*, vol. 45, no. 5, pp. 583–595, May 1997.
[32] J. Xu, L. Zhang, D. Zhang, and X. Feng, "Multi-channel weighted nuclear norm minimization for real color image denoising," in *Proc. IEEE Int. Conf. Comput. Vis.*, Oct. 2017, pp. 1096–1104.
[33] J. Miao and K. I. Kou, "Color image recovery using low-rank quaternion matrix completion algorithm," *IEEE Trans. Image Process.*, vol. 31, pp. 190–201, 2022.
[34] Y. Xu, L. Yu, H. Xu, H. Zhang, and T. Nguyen, "Vector sparse representation of color image using quaternion matrix analysis," *IEEE Trans. Image Process.*, vol. 24, no. 4, pp. 1315–1329, Apr. 2015.
[35] X. Xiao and Y. Zhou, "Two-dimensional quaternion PCA and sparse PCA," *IEEE Trans. Neural Netw. Learn. Syst.*, vol. 30, no. 7, pp. 2028–2042, Jul. 2018.
[36] R. Lan, Y. Zhou, and Y. Y. Tang, "Quaternionic Weber local descriptor of color images," *IEEE Trans. Circuits Syst. Video Technol.*, vol. 27, no. 2, pp. 261–274, Feb. 2017.
[37] X. Zhu, Y. Xu, H. Xu, and C. Chen, "Quaternion convolutional neural networks," in *Proc. Eur. Conf. Comput. Vis.*, 2018, pp. 631–647.
[38] L. Yang, J. Miao, and K. I. Kou, "Quaternion-based color image completion via logarithmic approximation," *Inf. Sci.*, vol. 588, pp. 82–105, Apr. 2022.
[39] C. Huang, Z. Li, Y. Liu, T. Wu, and T. Zeng, "Quaternion-based weighted nuclear norm minimization for color image restoration," *Pattern Recognit.*, vol. 128, Aug. 2022, Art. no. 108665.
[40] C. Huang, M. K. Ng, T. Wu, and T. Zeng, "Quaternion-based dictionary learning and saturation-value total variation regularization for color image restoration," *IEEE Trans. Multimedia*, vol. 24, pp. 3769–3781, 2022.
[41] K. Zhang, W. Zuo, and L. Zhang, "FFDNet: Toward a fast and flexible solution for CNN-based image denoising," *IEEE Trans. Image Process.*, vol. 27, no. 9, pp. 4608–4622, Sep. 2018.
[42] C. Liu, F. Wu, and X. Wang, "EFINet: Restoration for low-light images via enhancement-fusion iterative network," *IEEE Trans. Circuits Syst. Video Technol.*, vol. 32, no. 12, pp. 8486–8499, Dec. 2022.
[43] J. Liu, Y. Sun, X. Xu, and U. S. Kamilov, "Image restoration using total variation regularized deep image prior," in *Proc. IEEE Int. Conf. Acoust., Speech Signal Process. (ICASSP)*, May 2019, pp. 7715–7719.
[44] W. Xu, Q. Zhu, N. Qi, and D. Chen, "Deep sparse representation based image restoration with denoising prior," *IEEE Trans. Circuits Syst. Video Technol.*, vol. 32, no. 10, pp. 6530–6542, Oct. 2022.
[45] W. R. Hamilton, *Elements of Quaternions*. Harlow, U.K.: Longmans, 1866.
[46] F. Zhang, "Quaternions and matrices of quaternions," *Linear Algebra Appl.*, vol. 251, pp. 21–57, Jan. 1997.
[47] P. R. Girard and W. E. Baylis, "Quaternions, Clifford algebras and relativistic physics," *SIAM Rev.*, vol. 50, no. 2, p. 382, 2008.
[48] E. J. Candès and B. Recht, "Exact matrix completion via convex optimization," *Found. Comput. Math.*, vol. 9, no. 6, pp. 717–772, Dec. 2009.
[49] S. Gu, Q. Xie, D. Meng, W. Zuo, X. Feng, and L. Zhang, "Weighted nuclear norm minimization and its applications to low level vision," *Int. J. Comput. Vis.*, vol. 121, no. 2, pp. 183–208, Jan. 2017.
[50] Z. Kang, C. Peng, and Q. Cheng, "Robust PCA via nonconvex rank approximation," in *Proc. IEEE Int. Conf. Data Mining*, Nov. 2015, pp. 211–220.
[51] S. V. Venkatakrishnan, C. A. Bouman, and B. Wohlberg, "Plug-and-play priors for model based reconstruction," in *Proc. IEEE Global Conf. Signal Inf. Process.*, Dec. 2013, pp. 945–948.
[52] G. Xie, Z. Li, S. Bhattacharyya, and A. Mehmood, "Plug-and-play deblurring for robust object detection," in *Proc. Int. Conf. Vis. Commun. Image Process. (VCIP)*, Dec. 2021, pp. 1–5.
[53] A. M. Teodoro, J. M. Bioucas-Dias, and M. A. T. Figueiredo, "Image restoration and reconstruction using targeted plug-and-play priors," *IEEE Trans. Comput. Imag.*, vol. 5, no. 4, pp. 675–686, Dec. 2019.
[54] K. Zhang, Y. Li, W. Zuo, L. Zhang, L. Van Gool, and R. Timofte, "Plug-and-play image restoration with deep denoiser prior," *IEEE Trans. Pattern Anal. Mach. Intell.*, vol. 44, no. 10, pp. 6360–6376, Oct. 2022.
[55] K. Zhang, W. Zuo, and L. Zhang, "Deep plug-and-play super-resolution for arbitrary blur kernels," in *Proc. IEEE/CVF Conf. Comput. Vis. Pattern Recognit. (CVPR)*, Jun. 2019, pp. 1671–1681.
[56] H. Li et al., "A plug-and-play demosaicing and denoising method on mobile cameras," *Proc. SPIE*, vol. 12065, pp. 725–730, Nov. 2021.
[57] Z. Zha, X. Yuan, J. Zhou, C. Zhu, and B. Wen, "Image restoration via simultaneous nonlocal self-similarity priors," *IEEE Trans. Image Process.*, vol. 29, pp. 8561–8576, 2020.
[58] Z. Zha, X. Yuan, B. Wen, J. Zhang, J. Zhou, and C. Zhu, "Image restoration using joint patch-group-based sparse representation," *IEEE Trans. Image Process.*, vol. 29, pp. 7735–7750, 2020.
[59] Z. Zha, X. Yuan, B. Wen, J. Zhou, and C. Zhu, "Group sparsity residual constraint with non-local priors for image restoration," *IEEE Trans. Image Process.*, vol. 29, pp. 8960–8975, 2020.
[60] M. Xie, X. Liu, and X. Yang, "A nonlocal self-similarity-based weighted tensor low-rank decomposition for multichannel image completion with mixture noise," *IEEE Trans. Neural Netw. Learn. Syst.*, early access, May 11, 2022, doi: 10.1109/TNNLS.2022.3172184.
[61] E. Ryu, J. Liu, S. Wang, X. Chen, Z. Wang, and W. Yin, "Plug-and-play methods provably converge with properly trained denoisers," in *Proc. 36th Int. Conf. Mach. Learn.*, 2019, pp. 5546–5557.
[62] Z. Wang, A. C. Bovik, H. R. Sheikh, and E. P. Simoncelli, "Image quality assessment: From error visibility to structural similarity," *IEEE Trans. Image Process.*, vol. 13, no. 4, pp. 600–612, Apr. 2004.
[63] M. Rizkinia, T. Baba, K. Shirai, and M. Okuda, "Local spectral component decomposition for multi-channel image denoising," *IEEE Trans. Image Process.*, vol. 25, no. 7, pp. 3208–3218, Jul. 2016.
[64] S. Gu, L. Zhang, W. Zuo, and X. Feng, "Weighted nuclear norm minimization with application to image denoising," in *Proc. IEEE Conf. Comput. Vis. Pattern Recognit.*, Jun. 2014, pp. 2862–2869.
[65] S. Du, Y. Shi, G. Shan, W. Wang, and Y. Ma, "Tensor low-rank sparse representation for tensor subspace learning," *Neurocomputing*, vol. 440, pp. 351–364, Jun. 2021.
[66] J. Guo, H. Chen, Z. Shen, and Z. Wang, "Image denoising based on global image similar patches searching and HOSVD to patches tensor," *EURASIP J. Adv. Signal Process.*, vol. 2022, no. 1, pp. 1–20, Dec. 2022.
[67] M. Lebrun, M. Colom, and J.-M. Morel, "The noise clinic: A blind image denoising algorithm," *Image Process. Line*, vol. 5, pp. 1–54, Jan. 2015.
[68] G. Chen, F. Zhu, and P. A. Heng, "An efficient statistical method for image noise level estimation," in *Proc. IEEE Int. Conf. Comput. Vis. (ICCV)*, Dec. 2015, pp. 477–485.
[69] Y. Shen, Z. Wen, and Y. Zhang, "Augmented Lagrangian alternating direction method for matrix separation based on low-rank factorization," *Optim. Methods Softw.*, vol. 29, no. 2, pp. 239–263, 2014.
[70] F. Nie, Z. Hu, and X. Li, "Matrix completion based on non-convex low-rank approximation," *IEEE Trans. Image Process.*, vol. 28, no. 5, pp. 2378–2388, May 2018.
[71] F. Shang, J. Cheng, Y. Liu, Z. Luo, and Z. Lin, "Bilinear factor matrix norm minimization for robust PCA: Algorithms and applications," *IEEE Trans. Pattern Anal. Mach. Intell.*, vol. 40, no. 9, pp. 2066–2080, Sep. 2018.

[72] Z. Sun, F. Latorre, T. Sanchez, and V. Cevher, "A plug-and-play deep image prior," in *Proc. ICASSP - IEEE Int. Conf. Acoust., Speech Signal Process. (ICASSP)*, Jun. 2021, pp. 8103–8107.
[73] K. Dabov, A. Foi, V. Katkovnik, and K. Egiazarian, "Image denoising by sparse 3-D transform-domain collaborative filtering," *IEEE Trans. Image Process.*, vol. 16, no. 8, pp. 2080–2095, Aug. 2007.
[74] K. Dabov, A. Foi, V. Katkovnik, and K. Egiazarian, "Color image denoising via sparse 3D collaborative filtering with grouping constraint in luminance-chrominance space," in *Proc. IEEE Int. Conf. Image Process.*, vol. 1, Sep. 2007, pp. I-313–I-316.
[75] V. Lempitsky, A. Vedaldi, and D. Ulyanov, "Deep image prior," in *Proc. IEEE/CVF Conf. Comput. Vis. Pattern Recognit.*, Jun. 2018, pp. 9446–9454.

Tingting Xu received the B.S. degree from the School of Software, Zhengzhou University, Zhengzhou, China, in 2021. She is currently pursuing the M.S. degree with the School of Computer Science and Technology, Harbin Institute of Technology, Shenzhen, China. Her research interests include low-rank tensor methods for high-dimensional image processing problems.

Xiaoyu Kong received the B.Sc. degree in computer science from Jilin University in 2021. He is currently pursuing the master's degree with the Harbin Institute of Technology (Shenzhen). His research interests include computer vision and machine learning.

Qiangqiang Shen received the B.S. and M.S. degrees from the Harbin Institute of Technology, Harbin, China, in 2016 and 2018, respectively. He is currently pursuing the Ph.D. degree with the School of Electronics and Information Engineering, Harbin Institute of Technology, Shenzhen, China. His current research interests include pattern recognition and machine learning.

Yongyong Chen (Member, IEEE) received the B.S. and M.S. degrees from the Shandong University of Science and Technology, Qingdao, China, in 2014 and 2017, respectively, and the Ph.D. degree from the University of Macau, Macau, in 2020. He is currently an Assistant Professor with the School of Computer Science and Technology, Harbin Institute of Technology, Shenzhen, China. He has published more than 50 research papers in top-tier journals and conferences, including IEEE TRANSACTIONS ON IMAGE PROCESSING, IEEE TRANSACTIONS ON NEURAL NETWORKS AND LEARNING SYSTEMS, IEEE TRANSACTIONS ON MULTIMEDIA, IEEE TRANSACTIONS ON CIRCUITS AND SYSTEMS FOR VIDEO TECHNOLOGY, IEEE TRANSACTIONS ON GEOSCIENCE AND REMOTE SENSING, IEEE TRANSACTIONS ON COMPUTATIONAL IMAGING, IEEE JOURNAL OF SELECTED TOPICS IN SIGNAL PROCESSING, *Pattern Recognition*, and ACM MM. His research interests include image processing, data mining, and computer vision.

Yicong Zhou (Senior Member, IEEE) received the B.S. degree in electrical engineering from Hunan University, Changsha, China, and the M.S. and Ph.D. degrees in electrical engineering from Tufts University, Medford, MA, USA.

He is currently a Professor with the Department of Computer and Information Science, University of Macau, Macau, China. His research interests include image processing, computer vision, machine learning, and multimedia security.

Dr. Zhou is a fellow of the Society of Photo-Optical Instrumentation Engineers (SPIE) and was recognized as one of "World's Top 2% Scientists" on the Stanford University Releases List and one of "Highly Cited Researchers" in 2020. He received the Third Price of Macao Natural Science Award as a Sole Winner in 2020 and a co-recipient in 2014. He has been the leading Co-Chair of Technical Committee on Cognitive Computing in the IEEE Systems, Man, and Cybernetics Society since 2015. He serves as an Associate Editor for IEEE TRANSACTIONS ON NEURAL NETWORKS AND LEARNING SYSTEMS, IEEE TRANSACTIONS ON CIRCUITS AND SYSTEMS FOR VIDEO TECHNOLOGY, IEEE TRANSACTIONS ON GEOSCIENCE AND REMOTE SENSING, and four other journals.